Nanoscale Advances

ROYAL SOCIETY OF CHEMISTRY

PAPER

View Article Online
View Journal | View Issue

Cite this: *Nanoscale Adv.*, 2025, **7**, 155

Amphoteric β-cyclodextrin coated iron oxide magnetic nanoparticles: new insights into synthesis and application in MRI†

Federica Calsolaro, ‡[a] Francesca Garello, ‡[b] Eleonora Cavallari, [b] Giuliana Magnacca, [c] Mikhail V. Trukhan, [a] Maria Carmen Valsania,[c] Giancarlo Cravotto, [a] Enzo Terreno *[b] and Katia Martina *[a]

Received 22nd August 2024
Accepted 25th October 2024

DOI: 10.1039/d4na00692e

rsc.li/nanoscale-advances

This work presents a group of high-quality hydrophilic and negatively charged coated, iron oxide magnetic nanoparticles (MNPs) that have been prepared using a microwave-ultrasound-assisted protocol, and demonstrates the great impact that the synthetic strategy has on the resulting MNPs. The different coatings tested, including citric acid, carboxymethyl dextran and β-cyclodextrin (βCD)/citric acid have been compared and have shown good dispersibility and stability. The ability of βCD to maintain the inclusive properties of the coated MNPs has been proven as well as their cytocompatibility. An amino citrate-modified βCD is proposed and its capabilities as a flexible amphoteric adsorbing device have been studied. The NMR relaxometric properties of the coated MNPs have been investigated using field-cycling nuclear magnetic relaxation dispersion profiles. For the amino citrate-modified βCD system, the order of magnitude of the Néel relaxation time is in the typical range for superparamagnetic systems' reversal times, *i.e.*, 10^{-10}–10^{-7} s. The r_d value corresponds to the physical radius of the magnetic core, suggesting that, in this particular case, the coating does not prevent the diffusive motion of water molecules, which provide the basis for potential future magnetic resonance imaging (MRI) applications.

Introduction

Over the last few years, iron oxide magnetic nanoparticles (IOMNPs) have been intensively explored for use in biomedical applications.[1–3] This is due to their versatility in drug targeting,[4,5] gene delivery,[6,7] and several technological applications, such as magnetic resonance imaging (MRI),[8–10] magnetic hyperthermia,[11] tissue engineering, cell tracking and bioseparation.[12,13] MNPs need to be water-compatible in order to be used in biomedical applications.[14,15] Hydrophilicity can be induced by adding coating agents with a hydrophilic moiety that can bind the particle surface.[16] Moreover, MNP size, size distribution, shape, crystallinity, surface area and magnetic characteristics all influence biological performance.[17–19]

The requirements for new synthetic procedures that provide control over the size, morphology and nano/microstructure of particles are a considerable challenge in MNP preparation.[20–22] The sonochemical technique is a promising and innovative method that allows for better control of particle size distribution, which is often barely possible with conventional procedures.[21] The relevance of synthesizing IOMNPs using the ultrasound (US)-assisted coprecipitation technique has been extensively demonstrated.[23–26]

Careful studies to synthesize MNPs for use as adsorbents have recently been carried out because of their high adsorption capacity[27,28] and several examples of the use of functionalized MNPs as nano-carriers have been reported.[29–32] Coating agents have also been demonstrated to be highly impactful in enhancing the loading and controlling the release of organic molecules. For example, polymer-coated Fe_3O_4 MNPs have shown effective adsorption and desorption capacity for the loading and release of the drug Enalapril.[33] Incorporating β-cyclodextrin (βCD) in the coating of MNPs has garnered significant attention due to its unique host–guest inclusion complexation capabilities, facilitating enhanced loading and controlled release of organic molecules.[34–37] Notably, βCD's ability to form inclusion complexes expands the repertoire of active sites on MNP surfaces, allowing for versatile applications in targeted drug delivery and MRI contrast enhancement.[38–41] Organic linkers can be used to indirectly coat MNP surfaces

[a]*Department of Drug Science and Technology, University of Turin, Via P. Giuria 9, 10125 Turin, Italy. E-mail: katia.martina@unito.it*

[b]*Department of Molecular Biotechnology and Health Sciences, University of Turin, Piazza Nizza 44/bis, 10126 Turin, Italy. E-mail: enzo.terreno@unito.it*

[c]*Department of Chemistry and NIS Interdepartmental Centre, University of Turin, Via Pietro Giuria 7, 10125 Turin, Italy*

† Electronic supplementary information (ESI) available: Synthesis and characterization of products **1–3**, βCD Citr-NH_2 and carboxymethyl dextran, synthesis of MNPs, Transmission Electron Microscopy, sorption and inclusion capacity, relaxometric properties: R_2/R_1 ratio. See DOI: https://doi.org/10.1039/d4na00692e

‡ These authors contributed equally to this work.

with CDs.[30,42–44] Silanes are generally used as organic linkers because they are chemically stable and versatile.[45–47] However, the accurate control of layer quality, in terms of monolayer or multilayer formation, is a difficult task,[48] and the synthetic process entails several procedural steps.[49] Carboxylate anchoring groups have been proven to work well in ligand–exchange processes and are available for chemical functionalization.[50] Dextran-coated IOMNPs are the most widely used systems in medical applications,[51–54] and the transformation of dextran to carboxy-dextran has been proven to enhance the physico-chemical properties of nanoparticles.[55–59]

In addition, surface charge is an important factor that must be considered in MNP formulation. It is essential in preventing NP aggregation through electrostatic repulsion and influences the interaction of nanomaterials with cells and tissues. In general, cationic NPs enter cells with higher efficacy thanks to interactions with negative membrane cells. However, they tend to form large aggregates in the presence of plasma and have faster blood clearance than neutral particles. Negatively charged NPs are also massively incorporated by cells, but show higher stability in plasma, meaning that their biocompatibility is consequently improved and clearance is prevented.[60,61] Combining hydrophilic and negatively charged organic molecules and CDs, used as adsorbent systems, on NP surfaces therefore becomes an important challenge in the production of biotechnological nanosystems. However, to the best of our knowledge, only a few examples of the preparation and application of similar systems have been reported in the literature. Jayaprabha and Joy have reported the preparation of citrate-modified βCD-functionalized magnetite MNPs for the delivery of curcumin to a specific site using an external magnetic field. A recent experiment and density functional theory (DFT) study proved the system's efficacy as a nanocarrier for quercetin.[62,63] Monteiro *et al.*, have demonstrated the importance of combining sodium citrate with CDs to obtain coated MNPs with high Irinotecan loading.[64]

While MNPs find a home in various applications, they fulfil a particularly important role as contrast enhancers in MRI. Colloidal suspensions of MNPs are capable of providing both T_1- and T_2-weighted images,[65] and represent the most important class of T_2 contrast agents. Several studies have shown that size influences MR relaxivity and NP pharmacological features.[66] For this reason, the size-controlled synthesis of uniform NP dispersions is essential for the fine control of MR relaxivity.[67,68] Furthermore, coating nature and thickness have important effects on R_1 and R_2 relaxivities. Coating layers influence the diffusion of protons and chemical exchange processes. As coating thickness and hydrophobicity increase, R_2 and R_1 dramatically decrease.[69] In order to develop versatile magnetic nanomaterials for biomedical use in MRI, this work presents the preparation and characterization of a panel of coated MNPs, and a novel example of hydrophilic βCD-grafted MNPs has also been investigated. In addition to carboxymethyl dextran, native βCD and citric acid, we synthesized a modified βCD since recent focused on charged cyclodextrin highlight their potential in the biomedical field to improve the current state of diagnostics, therapeutics, and sensing technologies.[70] We hypothesize that a βCD derivative that covalently bind βCD and citric acid with a polyammino spacer can be exploited as a new generation of MNPs coating agent because being a flexible, amphiprotic adsorbing system, it can improve dispersibility, stability, and cytocompatibility of nanoparticles, making them promising candidates for advanced magnetic resonance imaging applications. We also accessed the necessity to careful optimize the syntheses of the coated MNPs, and the manuscript presents a careful optimization of the syntheses of the coated MNPs being them prepared conventionally and under MW/US irradiation. All devices were therefore characterized in detail, and adsorption capacity, stability in serum, and relaxometric properties were also investigated with a view to potential applications.

Results and discussion

The efficiency of MW irradiation in the production of MNPs is based on the technique's thermal and non-thermal effects, which produce nanoparticles with shorter reaction times.[71–73] Due to the fact that magnetic stirring is not advisable, and it is difficult to maintain reproducibility, simultaneous irradiation with MW and US is considered a powerful alternative to the use of MW alone. Although several manuscripts have already referred to the preparation of nanoparticles under synergic MW/US irradiation,[74–76] only one study refers to its application in MNP synthetic protocols to obtain a sorbent for vitamin D extraction.[77] Till now, no references reported the use of MW combined with US for preparation of MNPs of biomedical interest even if either MW irradiation and sonochemistry can both be considered efficient enabling technologies in this field. Based on the reported literature, we observed that one of the main limitation of the sonochemically assisted NPs preparation is the high variability of results due to differences in US probes and frequencies: as reported in 2015 by R. Dolores *et al.*, different iron oxide NPs are achieved by US irradiation alone because different frequencies provide differences in temperature and affects the cavitation efficiency.[78] We envisage synergic application of MW and US as a valuable opportunity to achieve a controlled and homogeneous temperature (MW) and to provide enhanced mass transfer (US) in the reaction medium. In fact, in order to circumvent common difficulties in controlling the size, morphology and structure of MNPs, MW/US irradiation can be used as a non-conventional strategy that provides efficient heating, dispersion and solid deagglomeration.

MNP preparation, particle size, polydispersity index, zeta potential

Co-precipitation is a popular and highly efficient method for synthesizing MNPs due to its simplicity, cost-effectiveness, and high yield for large-scale production, therefore preliminary bare MNPs were synthesized *via* aqueous coprecipitation using conventional and non-conventional techniques at 80 °C. Conventional heating and combined MW/US irradiation were compared, and TEM images confirmed that MNPs were more homogeneous in size distribution and shape when prepared

Table 1 Bare and coated MNP preparation: comparison of the different synthetic procedures[e]

Entry	MNPs	Synthetic procedure	Reaction cond.	PDI[a]	Size[b] [nm]
1	Bare MNPs	Co-precipitation	Oil bath (80 °C), 1.5 h	n.d.	6–15[c]
2			MW/US (80 °C), 30 min	n.d.	6–10[c]
3	MNPs@StA	Co-precipitation	Oil bath (60 °C), 24 h	0.24 ± 0.05[d]	114 ± 3[d]
4			MW/US (65 °C), 30 min	0.15 ± 0.04[d]	23.0 ± 0.9[d]
5	MNPs@CA	Physical assembly from bare MNPs (entry 2)	Oil bath (80 °C), 1 h	0.37 ± 0.03	40 ± 2
6			MW/US (80 °C), 30 min	0.34 ± 0.04	33 ± 2
7		Ligand exchange from MNPs@StA (entry 4)	Oil bath (50 °C), 12 h	0.187 ± 0.028	75 ± 2
8	MNPs@CMD	Physical assembly from bare MNPs (entry 2)	oil bath (80 °C), 1 h	0.2 + 0.05[b]	115 ± 3
9			MW/US (80 °C), 30 min	0.11 + 0.04[b]	69 ± 1
10		Ligand exchange from MNPs@StA (entry 4)	Oil bath (50 °C), 12 h	0.28 + 0.05	73 ± 1

[a] Polydispersity index acquired using DLS analyses. [b] Hydrodynamic diameter acquired using DLS analyses. [c] Diameter acquired using TEM analyses. [d] Polydispersity index of hexane suspensions of coated MNPs acquired using DLS analysis. MNPs@StA were analyzed as hexane suspensions due to their hydrophobic character. MNPs@CA were analyzed as water suspensions due to their hydrophilic character. [e] n.d. indicates 'not detectable', as the bare MNP suspensions are highly unstable due to the absence of coating.

using MW/US (see Table 1 and ESI Fig. S7A and B†). To achieve the best results, the instrument protocol was optimized to maximize the efficiency of combined MW and US irradiation. As depicted in Fig. S1,† the system integrated a Pyrex immersion horn and a multimodal MW oven: the horn operated at a frequency of 20 kHz with a power output of 30 W, and the sample temperature was set to 80 °C for 30 minutes under MW irradiation. As described in the graph of Fig. S2,† an average MW power of 46 W was continuously adsorbed by the sample demonstrating the simultaneous contribution of both technologies.

The preparation of stearic acid-coated magnetic nanoparticles (MNPs@StA) was optimized using the co-precipitation technique, with either MW/US or conventional heating, to develop lipophilic systems for phase-transfer protocols. The assembly of the magnetic iron oxide core and stearic acid occurs through interactions between the surfactant's terminal polar head and the nanoparticle surface. Reaction parameters were optimized to improve nanoparticle quality. Given the limitations of this method—such as aggregation, difficulty in controlling particle size and shape, and broad size distribution—the synergistic effects of MW and US were investigated. The temperature was maintained at 60–65 °C, as recommended in the literature for both conventional and non-conventional protocols.[79]

Subsequently, we compared the ligand–exchange approach and the chemical assembly to obtain core–shell nanostructured systems. Citric acid (CA) and carboxymethyl dextran (CMDx) were preliminarily used to coat and stabilize the NPs in solution with the aim of producing negatively charged hydrophilic MNPs suitable for MRI applications (Scheme 1).

The partition of MNPs@StA into the hexane and aqueous phases demonstrates the hydrophobicity of MNPs@StA, which mostly stays in the hexane phase (See ESI Fig. S3†). Treatment with hydrophilic molecules resulted in the complete partitioning of MNPs into the aqueous layer to achieve the ligand exchange.

The impact of the preparation technique on MNP features was investigated by monitoring the size, shape, morphology and surface hydrophilicity of the prepared nanoparticles using the

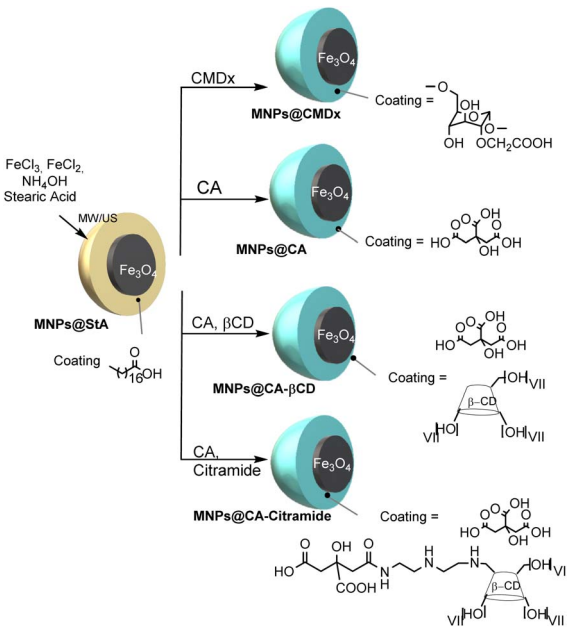

Scheme 1 Schematic representation of coated-MNP preparation.

Dynamic Light Scattering technique (DLS) to record the hydrodynamic diameters and diameter distribution of the systems, as well as their Transmission Electron Microscopy (TEM) and dispersibility in water. The efficacy of MW/US irradiation was demonstrated and more highly homogeneous and controlled systems were obtained compared to the conventionally prepared physically assembled MNPs (see Table 1). Lipophilic MNPs@StA, hydrophilic MNPs@CA and MNPs@CMDx showed smaller polydispersity indices (PDI) and hydrodynamic diameter when prepared under MW/US irradiation (see Table 1 entries 2, 4, 6, 7, 9 and 10). It was observed that the two synthetic strategies employed for the formation of coated MNPs, namely the ligand exchange approach and chemical assembly, exerted a considerable influence on the stability and dispersibility of the systems. As illustrated in

Fig. S4 (see ESI†), a range of MNPs were dispersed in water (4 mg mL^{-1}), and images of the bottom of the vials were captured at various time points to document the formation of precipitates.

Following a 12 hours period, it was observed that MNPs prepared *via* the ligand exchange approach remained well suspended in water, with no visible precipitation compared to MNPs prepared by physical assembly (see ESI, Fig. S4,† comparison between vials A–C and D–E). We could also observe that MNPs produced *via* physical assembly in an oil bath precipitated after four hours in water, while those assembled using MW/US irradiation demonstrated enhanced dispersibility, with precipitation occurring only after eight hours.

It is noteworthy that the MNPs produced through the ligand exchange approach exhibited the highest dispersibility. When these MNPs were coated with β-CD and CA (see ESI, Fig. S4,† vial E), only trace amounts of precipitate were visible at the bottom of the vial after 60 hours. This enhanced stability highlights their potential use as contrast agents in MRI.

Subsequently, MNPs@StA prepared un MW/US were exchanged with either a mixture of CA and βCD, or a mixture of CA and the amido derivative of βCD and citric acid (βCD-Citr-NH_2) to obtain MNPs@CA-βCD, and MNPs@CA-βCD-Citr-NH_2 (See Schemes 1 and 2). The strategy of adding βCDs to citric acid was pursued in order to obtain multifunctional nanocomposite MNPs and therefore meet the demand for biocompatible adsorbent nanomaterials. βCD was chosen because of its biocompatibility,[80] as well as its ability to increase adsorbent properties and to act as a vector by forming host–guest inclusion complexes. On the other hand, citric acid was essential to prevent MNP aggregation, through electrostatic repulsion. This combination is an important tool for the production of biotechnological nanosystems. As reported above, the citric amide of polyamino βCD was explored in a study of the influence of an amino citrate spacer between the MNP core and βCD, which is used to retain the high accessibility of the cyclodextrin cavity, while maintaining the ability of the carboxylate function to chemisorb to the MNPs. The preparation of βCD-Citr-NH_2 was carried out *via* a multistep synthetic scheme that yielded diethylenetriamine-βCD (compound **2** in Scheme 2) as a key intermediate.

Based on our previous experience, βCD was regioselectively tosylated in the presence of tosylimidazole to obtain tosyl-βCD (compound **1** in Scheme 2).[81,82] Diethylenetriamine-βCD (compound **2** in Scheme 2) was obtained *via* nucleophilic displacement and then reacted with citric anhydride (compound **3** in Scheme 2) to form a stable amide bond. Citric anhydride was prepared from citric acid in acetic anhydride acetic acid and obtained as a five-term cyclic anhydrides acetylated on the hydroxyl group, (see ESI†), it was reacted efficiently with βCD (compound **2** in Scheme 2) to afford the desired βCD-Citr-NH_2.

Fig. 1 depicts the ^1H and 2D HMQC NMR spectra of βCD-Citr-NH_2, which were obtained to substantiate the characterization of this conjugate. The HMQC enabled the detection of carbon and proton signals pertaining to the substituent on the CD. Furthermore, the HR-MS confirmed the identity of this derivative (see ESI,† Fig. S20). Also the isolated intermediates (**1** and **2**) were isolated and pure products and fully characterized; the data are presented in the ESI.†

MNPs@CA, MNPs@CMDx, MNPs@CA-βCD and MNPs@CA-βCD-Citr-NH_2, prepared by means of the phase-transfer protocol, were thoroughly characterized using the DLS, Transmission Electron Microscopy (TEM), thermogravimetric analysis (TGA), Fourier Transform Infrared (FT-IR) spectroscopy and zeta potential analysis.

As depicted in Table 2, all MNPs showed hydrodynamic diameters of <88 nm and polydispersity indices ranging from 0.18 to 0.33. Zeta potential analyses confirmed the formation of negatively charged NPs, with values ranging between −30.3 mV and −35.7 mV. Because of the presence of amino functionalities, MNPs@CA-βCD-Citr-NH_2 exhibited lower zeta potential than MNPs@CA and MNPs@CA-βCD. To demonstrate the effectiveness of non-conventional methods in the preparation of MNPs using βCD, MNPs@CA-βCD were synthesised by physical assembly from bare MNPs under both conventional

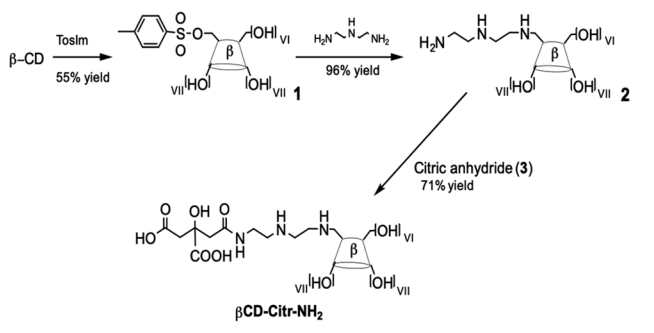

Scheme 2 Synthesis of amido derivative βCD-Citr-NH_2. (**1**) is tosyl-βCD, (**2**) is diethylenetriamine-βCD.

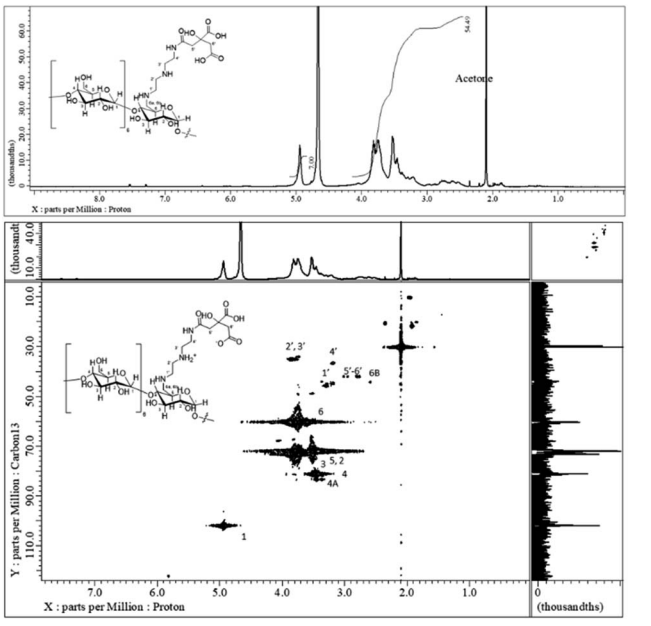

Fig. 1 ^1H NMR and HMQC (D_2O) βCD-Citr-NH_2. The derivative includes acetone that could not be removed under vacuum.

Table 2 Dispersibility, size, degree of functionalization and zeta potential

Entry	Product	PDI[a]	Size[b] [nm]	Coating[c] [w/w%]	Zeta potential[d] [mV]
1	MNPs@CA	0.187	75.0 ± 1.8 9.5 ± 0.2	16	−35.7 ± 0.9
2	MNPs@CMDx	0.284	73.0 ± 1.3 9.5 ± 0.2	33	−30.3 ± 1.4
3	MNPs@CA-βCD	0.228	86.0 ± 7.0 7.1 ± 0.2	33	−33.4 ± 2.1
4	MNPs@CA-βCD-Citr-NH_2	0.335	87.0 ± 1.6 7.1 ± 0.2	24	−30.6 ± 1.8

[a] Polydispersity index of hexane suspensions acquired from the DLS analysis of coated MNPs. [b] Hydrodynamic diameter size acquired from the DLS analysis and diameter size acquired from the TEM analysis. [c] Percentage of coating on MNP surfaces, measured using thermogravimetric analysis. [d] Zeta potential measured by DLS analysis.

and MW/US conditions. In addition, MNPs@CA-βCD were prepared by ligand exchange from MNPs@StA (MW/US preparation) and characterised by DLS and TGA. As described in Table S1 (ESI†) these enabling technologies produced negatively charged MNPs with smaller PDI and hydrodynamic diameters, consistent with previous findings for MNPs coated with CA or CMDx. We also explored the dispersibility and as shown in Fig. S5,† the non-conventional method significantly improved the dispersibility of the nanosystem in water compared to the conventional method. Considering that both methods used similar procedures and produce nanoparticles with comparable amounts of coating agent (22% and 25% w/w, as reported in Table S1†), the improved quality of MNPs prepared with MW/US either in terms of size or dispersibility, is evident.

TGA and FT-IR characterization

TGA analysis was used to demonstrate the presence of a coating layer on the MNP surfaces. The w/w% of coating/MNPs was calculated from the difference in residual weights of the bare and coated MNPs, and is reported in Table 2. The amount of coating varied substantially, from 16 to 33% (Fig. 2). Thermogravimetric analysis can also be used to evaluate the thermal stability of MNP systems, and these evaluations were performed in the temperature range of 100–800 °C under a nitrogen atmosphere. The profiles were normalized to 100 °C and the weight loss between 100 and 150 °C was ascribed to the evaporation of adsorbed water molecules.

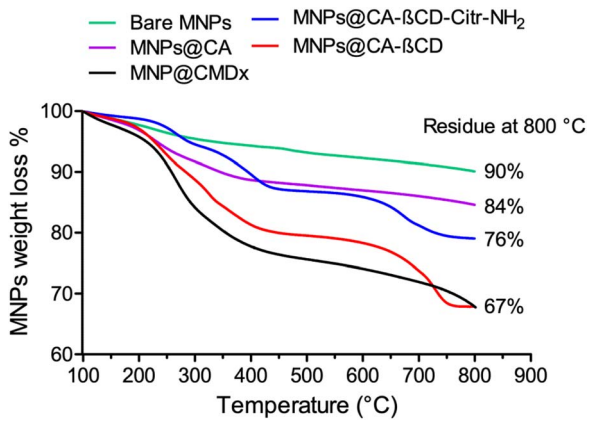

Fig. 2 TGA profiles of bare MNPs; MNPs@CA, MNPs@CMDx, MNPs@CA-Citr-βCD-NH_2 and MNPs@CA-βCD.

As shown in Fig. 2, TGA results display a single-step weight loss in MNPs@CA at 225 °C (onset temperature). As has already been reported in the literature,[83] the degradation temperature of CA is higher when present on coated MNPs than when in the pure form, which demonstrates that additional energy is requested to desorb the compound from the MNP. On the other hand, the TGA curve of MNPs@CMDx shows a main degradation phase with an inflection point at 270 °C. The degradation peak of coated MNPs is slightly lower than the temperature value registered in the pure CMDx degradation profile (~300 °C) due to the iron catalytic effect, which has been reported in the literature.[84] The TGA curves of MNPs@CA-βCD and MNPs@CA-βCD-Citr-NH_2 display three degradation steps: at 244 or 268, 323 or 396 and 729 or 668 °C, which can be ascribed to the decomposition of the solid supported β-CD.[85]

FT-IR studies were also performed to characterize the coating composition of the MNPs. The profiles of the FT-IT spectra of MNPs@StA, MNPs@CMDx, MNPs@CA and MNPs@CA-βCD are reported in Fig. 3. The FT-IR spectra show characteristic iron oxide magnetic core absorption bands at 610–580 cm^{-1}, which correspond to the torsional and stretching vibrations of the Fe–O bond.[86] The characteristic peaks of the surfactant are clearly visible in the MNPs@StA spectrum. Peaks at 2920 and 2850 cm^{-1} are ascribed to CH_2 symmetric and asymmetric stretching. The typical peaks attributed to OCO symmetric and asymmetric vibrational modes of carboxylic (and carbonate-like) functionalities are visible at 1555 and 1390 cm^{-1}. After the exchange with CA, the symmetric and asymmetric vibration peaks of the same group can be observed at 1603 cm^{-1} and 1407 cm^{-1}; both are shifted compared to pure CA, as it has already been reported in literature.[87] The signals at 3330–3220 cm^{-1} are assigned to the O–H stretching vibration of the hydroxyl groups exposed on the MNP surfaces or to physisorbed water.[88] When ligand exchange was performed with CMDx, CA-βCD or CA-βCD-Citr-NH_2, the FT-IR spectra show broad absorption peaks at 3300 cm^{-1}, indicating the presence of glucose O–H hydroxyl groups and, as depicted in Fig. S6 (See ESI†), both the MNPs@CA-βCD and MNPs@CA-βCD-Citr-NH_2 spectra resemble the βCD IR spectrum. The –COO– symmetric and antisymmetric stretching[89] of both CMDx and CA

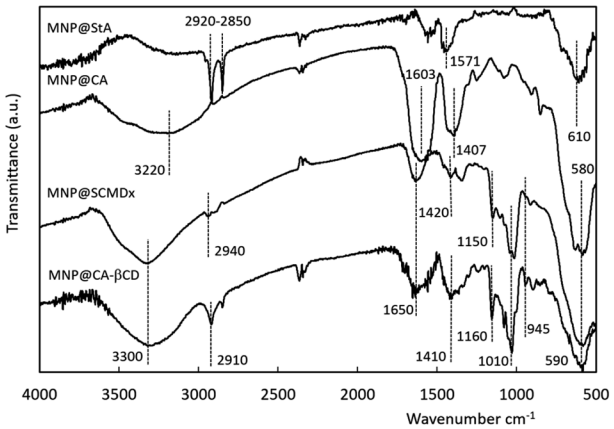

Fig. 3 FT-IR spectra of MNPs@StA, MNPs@CA, MNPs@CMDx, MNPs@CA-βCD. The curves have been shifted for the sake of clarity.

can be observed around 1650 cm^{-1} and at 1420 cm^{-1}. The asymmetric C–H stretching vibrations mean that the band at 2900 cm^{-1} is clearly observable when either βCD or CMDx are coating MNPs. Both CMDx and βCD have peaks at 1150–1000 cm^{-1} and these can be assigned to α-glucopyranose ring deformation modes,[90–92] while the peak at 1080 cm^{-1} is assigned to C–H vibration.

Transmission electron microscopy observations

The size and morphology of bare and coated MNPs were studied using HR-TEM analysis. The aggregation state and size of the resulting iron oxide nanoparticles changed depending on the approach employed to synthesize the nanosystems (see ESI Fig. S7†). In more detail, when bare MNPs were prepared following the co-precipitation method under conventional heating, larger particle sizes and more highly aggregated species were obtained compared to the bare MNPs obtained by combined MW and US irradiation (see Table 1 entries 1 and 2). In addition, the material resulting from the MW and US-assisted synthesis method showed uniform size and morphology, with a predominance of sphere-like particles in the nano dimensions (see ESI Fig. S7† A *versus* B). The same can be observed by analyzing the size and shape of the coated MNPs@CA, MNPs@CMDx, MNPs@CA-βCD and MNPs@CA-βCD-Citr-NH_2. Diameters of around 6–15 nm are observed and the nanoparticles have sphere-like morphology. In addition, the well-defined lattice fringes of the crystallographic planes of iron oxide species are visible in all of the samples, which helps nanoparticle identification and suggests that sample structure typology is crystalline (See Fig. 4). According to the literature, below a critical size, the number of magnetic domains decreases towards one, with this domain being characterized by a group of spins all pointing in the same direction and acting cooperatively. This is because, if particle size is limited, all the domain structures can easily align and act in a cooperative way, and thus increase the overall magnetization of the material.[93,94]

The HR-TEM image of MNPs@CA-βCD and a representative image of MNPs are shown in Fig. 4, with the sphere-like morphology of the NPs and the well-defined lattice fringes being visible. The interplanar distances were calculated and the obtained values correspond to the interplanar distances of the (227) planes of magnetite Fe_3O_4 (reference card 01-072-2303). These crystallographic planes belong to the Fe_3O_4 crystalline structure. The particle size distribution proves the uniformity of size and average radius of 7 nm. The HR-TEM images of all of the samples can be found in the ESI (see Fig. S7†).

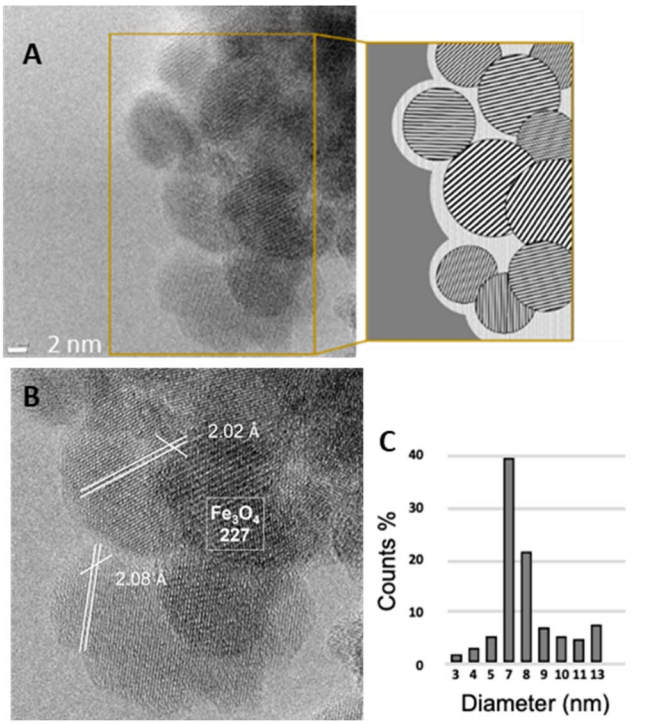

Fig. 4 (A) HR-TEM image of MNPs@CA-βCD, with a schematic representation of nanoparticle morphology and the alignment of the spacings between the observed diffraction fringes, which are directly visible in HR-TEM image (B). (C) Particle size distributions $n = 97$.

Sorption and Inclusion Capacity

To determine whether MNPs@CA-βCD and MNPs@CA-βCD-Citr-NH_2 can act as nanocarriers, phenolphthalein and adamantane amine were selected as appropriate hosts for the β-CD cavity (see Table 3 and Fig. 5).

The interaction between βCD and phenolphthalein (Php) was exploited to measure the amount of βCD that maintains inclusive properties on the MNPs surface. Above pH 8.4, Php has a distinctive purple color that is lost upon complexation with βCD.[95,96] UV-vis spectroscopy was used to quantify the βCD amount *via* measurements of the absorbance change of the UV Php peak at 553 nm in a 0.008 mM solution in basic buffer (pH 10.5) (see calibration curve ESI Fig S8†). When MNPs@CA-βCD was analyzed, the measured amount of βCD was 89 μmol g^{-1} (10.17 g/100 g). This result differs from the weight percentage measured in a TGA analysis of coated MNPs (33 w/w% see Table 2) because of the inability of all βCDs to act as inclusion vectors. An analysis of MNPs@CA-βCD-Citr-NH_2 confirmed the previous data and a comparable inclusion ability was observed; 87 μmol g^{-1} of βCD that was free and able to include Php was measured

Table 3 Phenolphthalein titration and sorption capacity data

Entry	MNPs	Inclusion capacity (mmol g^{-1} – w/w%)	Sorption capacity βCD (mmol g^{-1} – w/w%)
1	Bare MNPs		1.015–15.4
2	MNPs@CA-βCD	0.089–2.67	1.94–29.1
3	MNPs@CA-βCD-Citr-NH_2	0.087–2.67	1.92–29.0

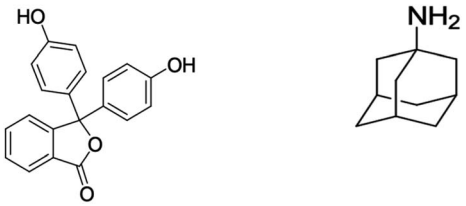

Fig. 5 Adsorbed molecules used for the study of MNPs@CA-βCD sorption capacity.

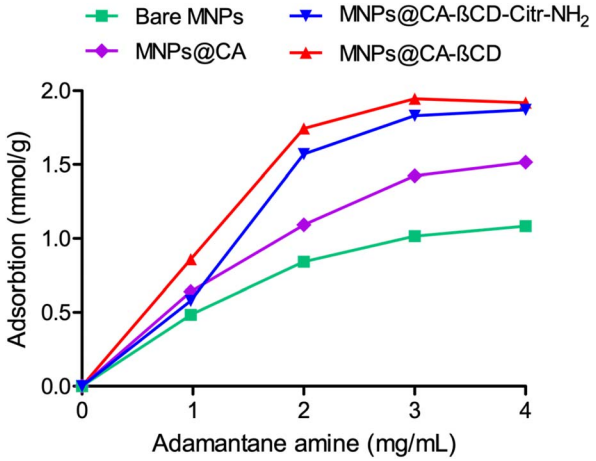

Fig. 6 Adsorption of adamantane amine onto bare MNPs, MNPs@CA, MNPs@CA-βCD, MNPs@CA-βCD-Citr-NH_2.

on the MNP surface, despite the 24% w/w registered by TGA. The inclusion capacity of MNPs@CA-βCD-NH_2 and MNPs@CA-βCD-Citr-NH_2 was around 2.67% (w/w), on the basis of inclusive properties of CD, for both derivatives (see Table 3).

Moreover, the capacity of the coated MNPs to adsorb adamantane amine was studied to give additional information on the surface properties of the material. The adsorbent was chosen to simulate nitrogen/amino-containing organic compounds since the electrostatic interaction between the citrate ion and the positively charged ammonium salt may affect and increase the adsorption capacity of CA-coated MNPs. In addition to ionic adsorption, βCD is capable of including adamantane, as has already been demonstrated in the literature, and improve its sorption capacity.[97] 2 mg of MNPs were added to 1 mL of adamantane amine solution (1 to 4 mg mL^{-1}) in ethanol : water (7 : 3), the suspension was gently sonicated and filtered solutions were analyzed by gas chromatography to determine capture efficiency (see calibration curve ESI Fig. S9†).

Bare MNPs showed moderate sorption capacity and an increase was observed in the presence of coated NPs (see Fig. 6). MNPs@CA demonstrated ionic interactions with the substrate and high affinity was observed with a maximum adsorbance of 1.51 mmol g^{-1} (23.0% w/w). A comparable adsorption capacity to that of MNPs@CA-βCD-Citr-NH_2 was detected for MNPs@CA-βCD; both coated MNPs were able to adsorb 1.94 mmol g^{-1} (approx. 300 mg g^{-1}). The improvement achieved in the presence of βCD confirmed the existence of two synergic interactions with adamantane amine either by acid base interaction with the acid coating or by the more selective host–guest inclusion complex with βCD cavity (see Fig. 6).

Magnetic measurements

The magnetic behavior of MNPs@StA, MNPs@βCD-CA and MNPs@CA-βCD-Citr-NH_2 was studied *via* magnetization measurements. Measured magnetization (M), in an applied field, H, is the cumulative response of a large number of particles. The measured $M(H)$ curve is, therefore, a statistical sum of the magnetization responses of individual MNPs with different domains and different phase compositions, which also depend on density, size and dipolar interactions.[98] Fig. 7 shows the magnetization curves of MNPs@βCD-CA and MNPs@CA-βCD-Citr-NH_2 at room temperature. Saturation magnetization generally increases with increasing MNP size, due to a decrease in cohesive energy, but is also dependent on the amount of non-magnetic matter surrounding the magnetic nanoparticle, the different chemical compositions of the surfaces, and surface effects on the magnetic field. The MS value for naked MNPs of similar size is approximately 90 emu g^{-1}. However, the addition of a non-magnetic functionalizing layer around the magnetic core results in a decrease in the MS value,[99,100] which in the case under study reaches a value of approximately 40 emu g^{-1}. This value is consistent with the reported values for similar MNPs, which typically range from 60 to 30 emu g^{-1}. As illustrated in Fig. 7, it was observed that MNPs@βCD-CA exhibited a diminished Ms value in comparison to MNPs@CA-βCD-Citr-NH_2 and MNPs@StA, which was attributed to the quantity of the coating agent. With regard to the coating w/w% as reported in Table 2 for MNPs@βCD-CA, the w/w ratio Fe_3O_4: coating is 1 : 0.33, whereas for MNPs@CA-βCD-Citr-NH_2 and MNPs@StA it is approximately 1 : 0.24. This serves to illustrate the impact of the coating agents on the surface magnetic anisotropy. The

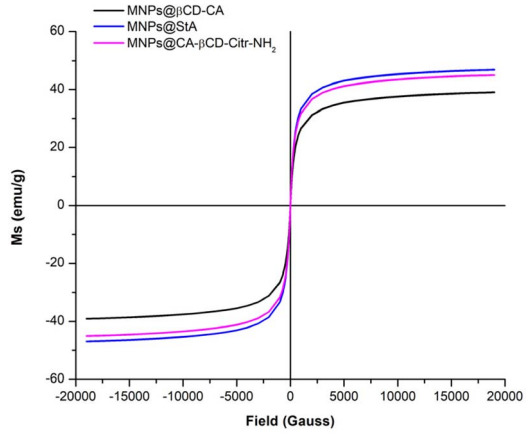

Fig. 7 Magnetization measurement analysis of MNPs@CA-βCD and CA-βCD-Citr-NH_2.

observed saturation magnetization values and the absence of a hysteresis loop are consistent with the superparamagnetic behavior of these systems.

Relaxometric properties

Given the promising applications of MNPs in MRI, we investigated the relaxometric properties of MNPs@CA, MNPs@CMDx, MNPs@CA-βCD and MNPs@CA-βCD-Citr-NH_2. Our study focused on the frequency-dependent behavior (0.01–70 MHz) of their longitudinal NMR relaxivity at physiological temperature (37 °C), commonly referred to as the NMR dispersion (NMRD) profile (Fig. 8).

This is a relevant tool for studying the magnetic properties of MNPs and assessing their potential as MRI contrast agents. To analyze these profiles, we employed the Roch's heuristic relaxation model,[101] with modifications, introduced by Lascialfari *et al.*,[102] specifically designed for MNPs with particle core diameters of below 20 nm.

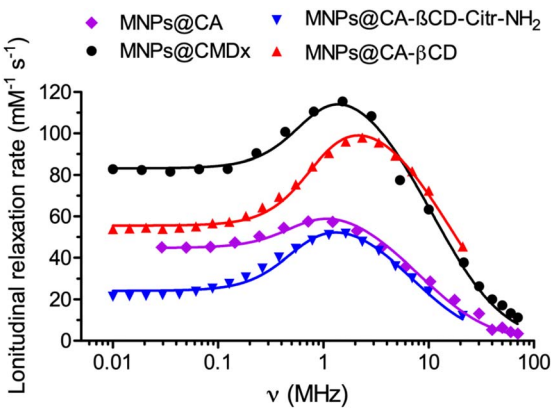

Fig. 8 NMRD profiles of MNPs@CMDx, MNPs@CA, MNPs@CA-βCD, MNPs@CA-βCD-Citr-NH_2, fitted using the heuristic Roch's model.

The standard error given by the algorithm is reported in parentheses. The previously discussed numerical values of MS and size obtained by TEM (Tables 1 and 2) were used as input data for the fitting procedure. MS values of MNPs@CA and MNPs@CMDx have not been measured and were obtained from the analysis.

Roch's heuristic model describes the longitudinal relaxation of a magnetic nanoparticle (MNP) suspension by considering two main factors. Firstly, it accounts for the diffusion of solvent protons into the inhomogeneous magnetic field generated by the large magnetic moment of the particles. This phenomenon, known as Curie relaxation, dominates at high frequencies. Secondly, the model incorporates the fluctuations of the electronic magnetic moment, referred to as Néel relaxation, which predominates at low frequencies. Néel relaxation is characterized by a relaxation time (τ_N^{NMR}), which represents the rate at which the magnetization orientation of the nanoparticles transitions from one direction along the axis of magnetization to the opposite direction. It is important to note that this reorientation time is assumed to be significantly shorter than the particle rotation correlation time.

At low frequencies, the spectral density that describes the behavior of 1H nuclear spin relaxation is given by the Freed function, which takes into account both Curie and Néel relaxations. However, at high frequencies, the magnetic moment aligns with the magnetic field direction, rendering Néel relaxation ineffective. In this regime, relaxation primarily occurs through water diffusion.

In this particular model, the longitudinal relaxivity is also affected by the particle size, represented by r_{NMR}, which corresponds to the average particle size measured by TEM, and r_d, the distance of minimum approach between water protons and the magnetic metallic core. r_d tends to r_{NMR} for uncoated naked particles, when water penetrates fully inside the coating. However, it is worth noting that r_d typically exceeds r_{NMR} in most cases.

The value of saturation magnetization (M_s) can be determined experimentally, as determined for MNPs@CA-βCD and MNPs@CA-βCD-Citr-NH_2 (Fig. 8), or through the analysis of the NMRD profiles using data collected at a high magnetic field.

Table 4 presents the results obtained from the analysis of the NMRD profiles of the MNPs examined herein.

The parameter r_{NMR} was varied within the range of radius measurements obtained by TEM. Interestingly, the r_{NMR} values for all of the nanosystems correspond to the maximum radius measured using this technique, thus suggesting that the nanoparticles interact with each other, forming clusters.

The parameter r_d, which indicates the minimum distance between a nanoparticle's magnetic core and the closest diffusing water molecule, plays a crucial role in determining water's characteristic diffusion time in relation to the nanoparticle. Since the coating affects the estimation of r_d, it is worth noting that the values obtained for MNPs@CA and MNPs@CMDx are similar and slightly larger than the core radius estimated by the model r_{NMR}. In the case of MNPs@CA-βCD, r_d is greater than the maximum radius measured *via* TEM. However, for the MNPs@CA-βCD-Citr-NH_2 system, the r_d value

Table 4 Best-fit parameters obtained by applying the heuristic Roch's equation to NMRD profiles

Sample	M_S (A m^2 kg^{-1})	r_{NMR} (nm)	r_d (nm)	τ_N^{NMR} (s)	P	Q
MNPs@CA	34 (19)	9.0 (0.5)	10.0 (0.5)	1.1 (8.3) × 10^{-7}	0.00 (0.08)	0.6 (1.0)
MNPs@CMDx	40 (30)	9.0 (0.3)	11.5 (0.4)	1.1 (5.0) × 10^{-7}	0.00 (0.07)	0.7 (0.8)
MNPs@CA-βCD	39.82	9.4 (0.3)	13.4 (2.2)	1.1 (5.4) × 10^{-8}	0.00 (0.08)	0.97 (2.8)
MNPs@CA-βCD-Citr-NH$_2$	45.79	7.8 (0.2)	8 (3)	1 (3) × 10^{-8}	0.00 (0.03)	0.9 (1.1)

corresponds to the physical radius of the magnetic core, suggesting that, in this particular case, the coating does not prevent the diffusive motion of water molecules.

The order of magnitude of the Néel relaxation time obtained by NMRD measurements, τ_N^{NMR}, is in the typical range for superparamagnetic systems' reversal times, *i.e.*, 10^{-10}–10^{-7} s.

Roch's heuristic equation does not explicitly include the activation energy barrier, and Roch *et al.*, have therefore derived a linear combination of the relaxivity equations for particles with zero magnetic anisotropy energy and those with infinite anisotropy. The coefficients for each equation are denoted as P and Q and act as weights for the contributions from the Zeeman energy and the activation energy barrier, respectively, while the constraints imposed were: that $0 < P < 1$, $0 < Q < 1$, $P + Q \leq 1$. P should decrease with increasing energy barrier while Q should increase because the magnetic anisotropy energy per particle increases proportionally with the volume of the magnetic core.

In all of the examined nanosystems, the P value approaches zero, and this result may be associated with the large size of the magnetic core.

In addition to the NMRD profiles, the samples were also characterized in terms of R_2/R_1 ratio, were R_2 corresponds to $1/T_2$ (T_2 is the transversal relaxation time) and R_1 corresponds to $1/T_1$ (T_1 is the longitudinal relaxation time). As shown in Fig. 8, the T_1 values at fields higher than 20 MHz are comparable for all of the investigated nanosystems, while the differences in the R_2/R_1 ratio reported in Fig. S10† can be ascribed to variations in the T_2 values alone. The highest R_2/R_1 value (close to 100) was observed at 70 MHz for MNPs@CA-Citr-NH$_2$, which consequently makes it a good candidate as a T_2 MRI contrast agent, especially at higher fields.

Stability assays

Important features must be considered for the application of NPs as contrast agents, delivery vectors for drug targeting and for similar biomedical applications. Particle size, charge, surface chemistry and functionalization are particularly important since they significantly affect blood circulation time, aggregation, mobility, and bioavailability within the body. Moreover, studies of stability and NP-aggregation levels under physiological conditions are of great importance. Here, the stability of MNPs in HEPES/NaCl buffer supplemented with 0.6 mM human albumin at 37 °C was investigated by relaxometric measurements performed at 0.5 T, which are sensitive to any changes in iron distribution or release. Relaxivity values were measured over four days at different time points. The results for MNPs@CMDx, MNPs@CA, MNPs@CA-βCD and MNPs@CA-βCD-Citr-NH$_2$ are shown in Fig. 9. All MNPs showed good stability in the time window tested.

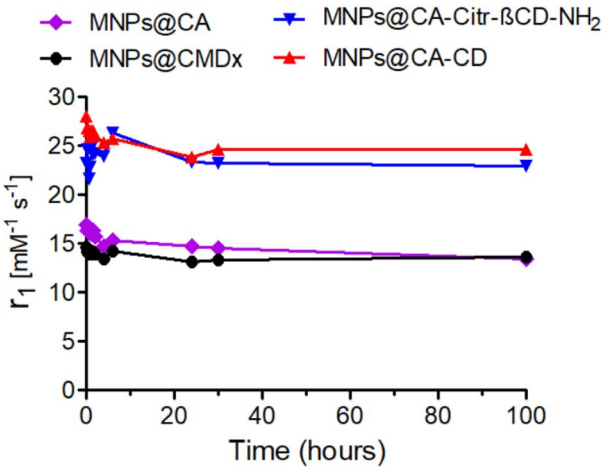

Fig. 9 Graphic representation of r_1 (mM^{-1} s^{-1}) stability of MNPs@CA, MNPs@CMDx, MNPs@CA-βCD-Citr-NH$_2$, MNPs@CA-βCD in albumin as a function of time (hours).

Cytotoxicity

In order to study the biocompatibility of the novel coated NPs MNPs@CA-βCD and MNPs@CA-βCD-Citr-NH$_2$, an MTT assay was performed following the incubation of J774A.1 cells with different concentrations of MNPs for different time periods (4 and 24 hours) (Fig. 10). J774A.1 cells are macrophages derived from the ascites of an adult mouse with reticulum cell sarcoma. Testing iron oxide nanoparticles on J774A.1 cells is crucial because these cells model macrophage behavior, which is critical in understanding the uptake, immune response, toxicity, and biological fate of nanoparticles. This information is essential for the development of safe and effective nanoparticle-based therapies, including those used in drug delivery, cancer treatment, and diagnostic imaging. The results obtained show that cell metabolism was affected in a concentration-dependent manner. MNP cytotoxicity increased with increasing iron concentration in both preparations. Moreover, cell viability varied slightly with MNP coating, demonstrating higher cytocompatibility when the cells were incubated with MNPs@CA-βCD-Citr-NH$_2$. Good sample cytocompatibility was demonstrated after 4 hours of incubation, even at 5 μg mL^{-1}, and cell viability was more than 70% at iron concentrations of 0.09 mM following 24 hours of incubation (5 μg mL^{-1}) for both MNPs@CA-βCD and MNPs@CA-Citramide. Carriers can be

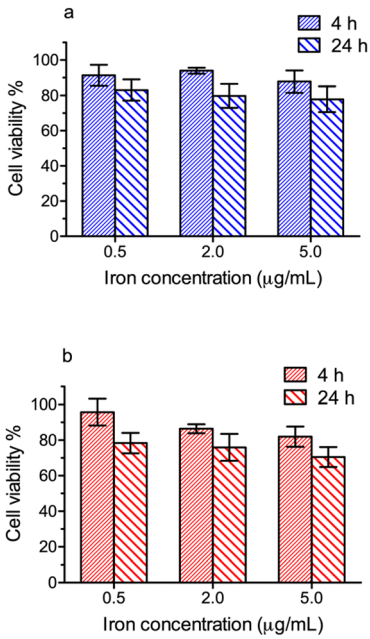

Fig. 10 MTT assay results for concentrations of 0.5, 2, 5 μg mL^{-1} of differently coated MNPs: [a] MNPs@CA-βCD-Citr-NH_2, [b] MNPs@CA-βCD.

considered non-cytotoxic as long as viability is higher than 70%, in accordance with ISO 10993-5:2009.[103]

Magnetic resonance imaging (MRI)

A proof of concept of the potential application of the synthesized MNPs as MRI contrast agents was performed. To this purpose J774A.1 cells were incubated with MNPs@CMDx, MNPs@CA, MNPs@CA-βCD and MNPs@CA-βCD-Citr-NH_2 (10 μg of MNPs per mL) for 4 hours. Cells incubated with culture medium only were used as controls. After 4 hours, the cells were profusely washed with PBS, detached and collected into glass capillary tubes. An agar phantom containing the tubes was prepared and cell pellets were imaged using MR at 1 and 7 T. As displayed in Fig. 11, a simple and fast T_2-weighted image was sufficient to visualize negative contrast in the cell pellets incubated with all the investigated MNPs. Additional studies concerning, for example sample dilutions, the minimum number of detectable labelled cells, and amount of internalized contrast agent are beyond the scope of this work and will be investigated in the context of a more biological study.

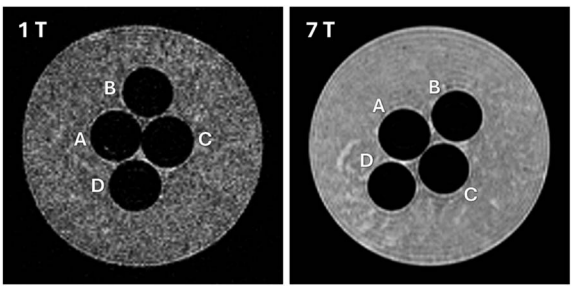

Fig. 11 T_2-weighted MRI acquired at 1 and 7 tesla of J774A.1 cells incubated for 4 hours with MNPs@CMDx (A), MNPs@CA (B), MNPs@CA-βCD (C), and MNPs@CA-βCD-Citr-NH_2 (D) at a concentration of 10 μg MNPs mL^{-1} of culture medium.

Conclusions

A simple, effective, and efficient, MW/US-assisted protocol for obtaining negatively charged MNPs is reported herein. The study demonstrates that enabling technologies provide control over the size, morphology, and nanostructure of particles. The ligand–exchange approach has been observed to be the most convenient and a set of high-quality coated MNPs have been synthesized. In addition to citric acid and carboxymethyl dextran, βCD was selected as a component of the NP coating to exploit its biocompatibility and its inclusive properties. Moreover, the results obtained support the hypothesis that an amino citrate-modified βCD can be exploited as a flexible charged amphoteric adsorbing device for the development of novel MNPs and confirm the potential of the new MNPs presented, especially for future preclinical MRI diagnostic and theranostic applications.

Experimental sections

In the ESI† Material methods are described, methods for the preparation of all coated MNPs, as well as synthesis and characterization of products **1–3** and βCD Citr-NH_2

Preparation of MNPs@CA-βCD

MNPs@StA (100 mg) were finely dispersed in 50 mL of petroleum ether. Citric acid (100 mg) and βCD (200 mg) were dissolved in 50 mL of deionized water. The solutions were combined and 0.5 mL of NaOH 1 N were added. The mixture was vigorously stirred at 50 °C for 12 h. The organic layer was removed, and the MNPs were collected from the aqueous phase using an external magnet, rinsed with deionized water and acetone, and dried under vacuum.

Preparation of MNPs@CA-βCD-Citr-NH_2

MNPs@StA (100 mg) were finely dispersed in 50 mL of petroleum ether. Citric acid (100 mg) and βCD citrate (citramide or Citr-NH_2) (244 mg) were dissolved in 50 mL of deionized water. The solutions were combined and 0.5 mL of NaOH 1 N were added. The mixture was vigorously stirred at 50 °C for 12 h. The organic layer was removed, and the MNPs were collected from the aqueous phase using an external magnet, rinsed with deionized water and acetone, and dried under vacuum.

Relaxometric characterization

The r_{1p} nuclear magnetic relaxation dispersion profiles (NMRD) of all the preparations were measured over a continuum of magnetic field strengths from 0.00024 to 0.5 T (corresponding to 0.01–20 MHz proton Larmor frequencies), on the fast field cycling (Stelar Spinmaster FFC 2000 relaxometer) equipped with a resistive low inductance air cored solenoid, made of silver and

used in Fast Field Cycling NMR relaxometers. r_{1p} values were calculated as follows:

$$r_{1p} = \frac{R_{1obs} - R_{1dia}}{[Fe^{3+}]}$$

where R_{1obs} is the inverse of the longitudinal relaxation time T_1, R_{1dia} is the diamagnetic contribution and $[Fe^{3+}]$ is the iron concentration of each sample, determined using the glass vial test.[51] For this purpose, aliquots of each sample were diluted 1 : 10 with HNO_3 (70% w/w), transferred to glass ampoules and centrifuged for 3 min at 2000 rpm. The glass vials were sealed and placed at 120 °C overnight to mineralize the samples. The longitudinal relaxation rate (R_{1obs}) was then measured at 21.5 MHz (0.5 T) and 25 °C. The millimolar concentration of Fe(III) was determined as follows:

$$[Fe^{3+}] = \frac{R_{1obs} - R_{1dia}}{18.47} \times 10$$

where R_{1dia} ($R_{1dia} = 0.481\ s^{-1}$) is the diamagnetic contribution under acidic conditions, while 18.47 $mM^{-1}\ s^{-1}$ is the relaxivity (r_1) of the Fe(III) aqua ion under acidic conditions at 21.5 MHz and 25 °C.

The relaxometer operates under complete computer control with an absolute uncertainty in the $1/T_1$ values of ±1%. T_1 was determined using the saturation recovery method. 16 values of delay between pulses were used. The number of averaged experiments was 2. Water proton T_1 measurements were carried out at a fixed frequency on a Stelar Spin Master Spectrometer [Stelar S.n.c., Mede (PV), Italy] operating in the 20 to 80 MHz range and using the inversion recovery method (16 delays values, two averages). Water proton T_1 and T_2, and the respective R_1 and R_2, were measured using a Stelar Spinmaster FFC 2000 relaxometer at 25 °C, from 21.5 to 70 MHz.

Stability assays

To check the stability of the prepared suspensions, longitudinal relaxation rate r_{1p} measurements (21.5 MHz, 25 °C) were carried out using a Stelar Spinmaster spectrometer at different time points for four days. The temperature was controlled using a Stelar VTC-91 airflow heater (Stelar srl, Italy), equipped with a copper-constantan thermocouple (uncertainty ± 0.1 °C). The preparations were diluted 1 : 1 in HEPES/NaCl buffer (300 mOsm, pH 7.3) supplemented with 1.2 mM albumin (final concentration 0.6 mM). For relaxometric measurements, the resulting samples (80 μL total volume) were transferred in sealed NMR tubes and kept at 37 °C in a Thermomixer (EchoTherm™ SC20 Orbital Mixing Chilling/Heating Dry Bath, Torrey Pines Scientific) under gentle vortexing (level 2) from day 0 to day 4. Before each measurement, the samples were kept at room temperature for 5 minutes to reach 25 °C.

Cytotoxicity assay

The cytotoxicity assay was carried out on the J774A.1 cell line (ATCC LGC Standards, Sesto San Giovanni, Italy). The cells were cultured in DMEM supplemented with 10% (v/v) FBS, 2 mM L-glutamine, 100 U mL^{-1} penicillin, and 100 μg mL^{-1} streptomycin at 37 °C in a humidified atmosphere with 5% CO_2. Cytotoxicity was evaluated using the MTT ((3-(4,5-dimethylthiazol-2-yl)-2,5-diphenyl-2H-tetrazolium bromide)) test.[104] To this purpose, 7×10^3 cells were plated in a 96-well plate. 24 hours after the medium was removed and the cells were incubated with growing concentrations of either MNPs@CA-βCD or MNPs@CA-βCD-Citr-NH_2 (iron concentration of 0.5, 2 or 5 μg mL^{-1}) in culture medium. Control cells were incubated with the culture medium and a volume of HEPES buffer corresponding to the volume of MNPs added, at 37 °C and 5% CO_2. After 4 and 24 hours the medium was removed, cells were washed five times with PBS and the MTT solution was added (0.454 mg mL^{-1} medium). Cells were incubated again at 37 °C for 4 hours, the MTT solution was then aspirated and 150 μL of DMSO was added to each well to dissolve the precipitated formazan. The microplate was then incubated at room temperature for 30 min. Finally, absorbance was read at 570 nm using an iMark microplate reader (Biorad). Cell vitality was reported as the percentage of dead cells observed in treated samples relative to that observed in control cells. The experiment was performed in triplicate and data are graphically presented as mean ± SD.

Magnetic resonance imaging (MRI)

For the MRI proof of concept, 1×10^6 J774A.1 cells were plated in 60 mm Petri dishes. 24 hours later, the medium was removed and the cells were incubated with 2 mL of culture medium containing either MNPs@CMDx, MNPs@CA, MNPs@CA-βCD or MNPs@CA-βCD-Citr-NH_2 (10 μg of MNPs per mL, corresponding to 4.0, 2.1, 3.2 and 3.2 μg iron per mL respectively) for 4 hours. Control cells were incubated with the culture medium only. After 4 hours the cells were profusely washed in PBS, detached with a scraper, and collected in PBS. After three additional washing cycles, the cells were resuspended in 50 μL of PBS and transferred into glass capillary tubes. After centrifugation at 600 rpm for 7 minutes, the capillary tubes were transferred into an agar phantom and imaged at 1 and 7 T. After the acquisition of a scout image, an axial T_2 weighted image of the samples was acquired using the following parameters: repetition time (TR) 4000 ms, Echo Time (TE) 3.9 ms, effective TE 31.3 ms, Rare Factor (RF) 16, number of averages 6, total acquisition time 3 min and 12 s, Field Of View (FOV) 1.2 cm × 1.2 cm, matrix 128 × 128, slice thickness 0.8 mm.

Data availability

The data supporting this article have been included in the manuscript and in the ESI.†

Author contributions

F. C. conceptualization, investigation, writing – original draft; F. G. conceptualization, investigation, writing – original draft; E. C. conceptualization, formal analysis, investigation; G. M. formal analysis, review and editing; M. V. T. formal analysis, investigation; M. C. V. formal analysis, investigation; G. C.

review and editing, supervision; E. T. conceptualization, writing – review and editing, supervision, project administration, K. M. conceptualization, writing – review and editing, supervision, project administration. All authors have given approval to the final version of the manuscript.

Conflicts of interest

The authors declare no competing financial interest.

Acknowledgements

The work has been performed with the support of the FOE contribution of the Italian Ministry of Research to the Euro-BioImaging MultiModal Molecular Imaging Italian Node (**www.mmmi.unito.it**). This research was also performed in the framework of COST Action AC15209 (EURELAX).

Notes and references

1 W. Wu, C. Z. Jiang and V. A. L. Roy, *Nanoscale*, 2016, **8**, 19421–19474.
2 J. Nowak-Jary and B. Machnicka, *J. Nanobiotechnol.*, 2022, **20**, 305.
3 K. Kritika and I. Roy, *Adv. Mater.*, 2022, **3**, 7425–7444.
4 T. Vangijzegem, D. Stanicki and S. Laurent, *Expet Opin. Drug Deliv.*, 2019, **16**, 69–78.
5 D. Stanicki, T. Vangijzegem, I. Ternad and S. Laurent, *Expet Opin. Drug Deliv.*, 2022, **19**, 321–335.
6 Q. Xu, T. Zhang, Q. Wang, X. Jiang, A. Li, Y. Li, T. Huang, F. Li, Y. Hu, D. Ling and J. Gao, *Int. J. Pharm.*, 2018, **552**, 443–452.
7 S. Yildiz, K. Solak, M. Acar, A. Mavi and Y. Unver, *Nanoscale Adv.*, 2021, **3**, 4482–4491.
8 C. Sun, J. S. H. Lee and M. Zhang, *Adv. Drug Deliv. Rev.*, 2008, **60**, 1252–1265.
9 Z. Shen, A. Wu and X. Chen, *Mol. Pharm.*, 2017, **14**, 1352–1364.
10 A. Avasthi, C. Caro, E. Pozo-Torres, M. P. Leal and M. L. García-Martín, *Top. Curr. Chem.*, 2020, **378**, 40.
11 M. R. Ruggiero, S. G. Crich, E. Sieni, P. Sgarbossa, M. Forzan, E. Cavallari, R. Stefania, F. Dughiero and S. Aime, *Nanotechnology*, 2016, **27**, 1–27.
12 V. I. Shubayev, T. R. Pisanic and S. Jin, *Adv. Drug Deliv. Rev.*, 2009, **61**, 467–477.
13 Y. Chen and S. Hou, *Stem Cell Res. Ther.*, 2022, **13**, 135.
14 A. K. Gupta and M. Gupta, *Biomaterials*, 2005, **26**, 3995–4021.
15 R. Nisticò, F. Cesano and F. Garello, *Inorganics*, 2020, **8**, 6.
16 A. M. Tomoiaga, A. Vasile, M. Alexandroaei and I. Sandu, *J. Optoelectron. Adv. Mater.*, 2014, **16**, 221–226.
17 S. Laurent, D. Forge, M. Port, A. Roch, C. Robic, L. Vander Elst and R. N. Muller, *Chem. Rev.*, 2010, **110**, 2574.
18 C. Xu and S. Sun, *Adv. Drug Deliv. Rev.*, 2013, **65**, 732–743.
19 S. Keshri and S. Biswas, *Prog. Biomater.*, 2022, **11**, 347–372.
20 G. Mirabello, J. J. M. Lenders and N. A. J. M. Sommerdijk, *Chem. Soc. Rev.*, 2016, **45**, 5085–5106.
21 Y. Wang, I. Nkurikiyimfura and Z. Pan, *Chem. Eng. Commun.*, 2015, **202**, 616–621.
22 M. Jena and S. Patil, *Eur. J. Biomed. Pharmaceut. Sci.*, 2022, **9**, 220–226.
23 S. Arsalani, Y. Hadadian, E. E. Mazon, E. J. Guidelli, E. Kava, A. P. Ramos, A. J. Gualdi, T. Z. Pavan, O. Baffa and A. A. O. Carneiro, *J. Magn. Magn. Mater.*, 2022, **564**, 170091.
24 S. Theerdhala, S. Vitta and D. Bahadur, *Mater. Technol.*, 2008, **23**, 88–93.
25 K. S. Suslick and G. J. Price, *Annu. Rev. Mater. Sci.*, 1999, **29**, 295.
26 X. Liu, Z. Wu, R. Cavalli and G. Cravotto, *Ind. Eng. Chem. Res.*, 2021, **60**, 10011–10032.
27 S. Wang, E. Li, Y. Li, J. Li, Z. Du and F. Cheng, *ChemistrySelect*, 2020, **5**, 4285–4291.
28 S. Chen and F. Xie, *Appl. Surf. Sci.*, 2020, **507**, 145090.
29 K. Hayashi, K. Ono, H. Suzuki, M. Sawada and M. Moriya, *ACS Appl. Mater. Interfaces*, 2010, **2**, 1903–1911.
30 T. Skorjanc, F. Benyettou, J.-C. Olsen and A. Trabolsi, *Chem.–Eur. J.*, 2017, **23**, 8333–8347.
31 L. Shi, J. Cao, C. Yang, X. Wang, K. Shi and L. Shang, *J. Colloid Interface Sci.*, 2022, **615**, 408–416.
32 A. Grayston, Y. Zhang, M. Garcia-Gabilondo, M. Arrue, A. Martin, P. Kopcansky, M. Timko, J. Kovac, O. Strbak, L. Castellote, S. Belloli, R. M. Moresco, M. Picchio, A. Roig and A. Rosell, *J. Cerebr. Blood Flow Metabol.*, 2022, **42**, 237–252.
33 N. Shahverdi, A. Heydarinasab, A. Panahi and E. Moniri, *ChemistrySelect*, 2019, 5246–5250, DOI: **10.1002/slct.201900697**.
34 L. Wang, L.-l. Li, Y.-s. Fan and H. Wang, *Adv. Mater.*, 2013, 3888–3898, DOI: **10.1002/adma.201301202**.
35 J. Nayak, K. S. Prajapati, S. Kumar, V. K. Vashistha, S. K. Sahoo and R. Kumar, *Mater. Today Commun.*, 2022, **33**, 104644.
36 H. Li, E. Peng, F. Zhao, J. Li and J. Xue, *Pharmaceutics*, 2021, **13**, 1884.
37 X. Hai, L. Ma, Y. Zhu, Z. Yang, X. Li, M. Chen, M. Yuan, H. Xiong, Y. Gao, F. Shi and L. Wang, *Carbohydr. Polym.*, 2023, **321**, 121295.
38 J. Ju, D. Xu, X. Mo, J. Miao, L. Xu, G. Ge, X. Zhu and H. Deng, *Carbohydr. Polym.*, 2023, **317**, 121048.
39 M. Hasani, S. Jafari, H. Akbari Javar, H. Abdollahi and H. Rashidzadeh, *ACS Appl. Bio Mater.*, 2023, **6**, 1019–1031.
40 Y. He, Z. Mao, Z. Lu, J. Yan, Y. Zhang, A. Bianco, Y. Cao and R. Pei, *ACS Appl. Nano Mater.*, 2022, **5**, 15826–15836.
41 E. Einafshar, H. Javid, H. Amiri, H. Akbari-Zadeh and S. I. Hashemy, *Carbohydr. Polym.*, 2024, **340**, 122328.
42 R. Selvam, S. Ramasamy, S. Mohiyuddin, I. V. M. V. Enoch, P. Gopinath and D. Filimonov, *Mater. Sci. Eng. C*, 2018, **93**, 125–133.
43 S. Ramasamy, B. Samathanam, H. Reuther, M. N. M. S. Adyanpuram, I. V. M. V. Enoch and K. Potzger, *Colloids Surf., B*, 2018, **161**, 347–355.
44 K. Kaliyamoorthi, A. Sumohan Pillai, A. Alexander, S. Ramasamy, A. Arivarasu and I. V. M. V. Enoch, *J. Mater. Sci.*, 2021, **56**, 3925–3934.

45 X. Sun, B. Dong, H. Xu, S. Xu, X. Zhang, Y. Lin, L. Xu, X. Bai, S. Zhang and H. Song, *ACS Appl. Mater. Interfaces*, 2017, **9**, 11451–11460.
46 E. Sattarzadeh, M. M. Amini, S. Kakaei and A. Khanchi, *J. Radioanal. Nucl. Chem.*, 2018, **317**, 1333–1339.
47 M. Yamaura, R. L. Camilo, L. C. Sampaio, M. A. Macêdo, M. Nakamura and H. E. Toma, *J. Magn. Magn. Mater.*, 2004, **279**, 210–217.
48 Y. Liu, Y. Li, X.-M. Li and T. He, *Langmuir*, 2013, **29**, 15275–15282.
49 X.-Y. Wang, D. Mertz, C. Blanco-Andujar, A. Bora, M. Ménard, F. Meyer, C. Giraudeau and S. Bégin-Colin, *RSC Adv.*, 2016, **6**, 93784–93793.
50 X. Wan, Y. Song, N. Song, J. Li, L. Yang, Y. Li and H. Tan, *Carbohydr. Res.*, 2016, **419**, 33–40.
51 D. J. Grootendorst, J. Jose, R. M. Fratila, M. Visscher, A. H. Velders, B. Ten Haken, T. G. Van Leeuwen, W. Steenbergen, S. Manohar and T. J. Ruers, *Contrast Media Mol. Imaging*, 2013, **8**, 83–91.
52 N. Zeng, L. He, L. Jiang, S. Shan and H. Su, *Carbohydr. Res.*, 2022, **520**, 108632.
53 S. Gao, R. M. Torrente-Rodriguez, M. Pedrero, J. M. Pingarron, S. Campuzano, J. Rocha-Martin and J. M. Guisan, *Talanta*, 2022, **247**, 123549.
54 M. J. Molaei, *J. Cryst. Growth*, 2023, **611**, 127186.
55 J. Pinkernelle, U. Teichgraeber, F. Neumann, L. Lehmkuhl, J. Ricke, R. Scholz, A. Jordan and H. Bruhn, *Magn. Reson. Med.*, 2005, **53**, 1187–1192.
56 O. Lunov, T. Syrovets, B. Büchele, X. Jiang, C. Röcker, K. Tron, G. U. Nienhaus, P. Walther, V. Mailänder, K. Landfester and T. Simmet, *Biomaterials*, 2010, **31**, 5063–5071.
57 P. Reimer and T. Balzer, *Eur. Radiol.*, 2003, **13**, 1266–1276.
58 A. Sharma, C. Cornejo, J. Mihalic, A. Geyh, D. E. Bordelon, P. Korangath, F. Westphal, C. Gruettner and R. Ivkov, *Sci. Rep.*, 2018, **8**, 4916.
59 C. Mandawala, I. Chebbi, M. Durand-Dubief, R. Le Fèvre, Y. Hamdous, F. Guyot and E. Alphandéry, *J. Mater. Chem. B*, 2017, **5**, 7644–7660.
60 C. Schweiger, R. Hartmann, F. Zhang, W. J. Parak, T. H. Kissel and P. Rivera-Gil, *J. Nanobiotechnol.*, 2012, **10**, 1.
61 Q. Feng, Y. Liu, J. Huang, K. Chen, J. Huang and K. Xiao, *Sci. Rep.*, 2018, **8**, 1–13.
62 K. N. Jayaprabha and P. A. Joy, *RSC Adv.*, 2015, **5**, 22117–22125.
63 R. Ghafelehbashi, M. Tavakkoli Yaraki, L. Heidarpoor Saremi, A. Lajevardi, M. Haratian, B. Astinchap, A. M. Rashidi and R. Moradian, *Mater. Sci. Eng., C*, 2020, **109**, 110597.
64 A. P. F. Monteiro, L. D. Caminhas, J. D. Ardisson, R. Paniago, M. E. Cortés and R. D. Sinisterra, *Carbohydr. Polym.*, 2017, **163**, 1–9.
65 D. Press, *Int. J. Nanomed.*, 2015, 1727–1741.
66 A. Joos, N. Löwa, F. Wiekhorst, B. Gleich and A. Haase, *J. Magn. Magn. Mater.*, 2017, **427**, 122–126.
67 E. Terreno, D. D. Castelli, A. Viale and S. Aime, *Chem. Rev.*, 2010, **110**, 3019–3042.
68 B. H. Kim, N. Lee, H. Kim, K. An, Y. I. Park, Y. Choi, K. Shin, Y. Lee, S. G. Kwon, H. B. Na, J.-G. Park, T.-Y. Ahn, Y.-W. Kim, W. K. Moon, S. H. Choi and T. Hyeon, *J. Am. Chem. Soc.*, 2011, **133**, 12624–12631.
69 L. E. W. Laconte, N. Nitin, O. Zurkiya, D. Caruntu, C. J. O. Connor and X. Hu, *J. Magn. Reson. Imag.*, 2007, **1641**, 1634–1641.
70 V. Sehgal, S. P. Pandey and P. K. Singh, *Carbohydr. Polym.*, 2024, **323**, 121348.
71 R. Y. Hong, T. T. Pan and H. Z. Li, *J. Magn. Magn. Mater.*, 2006, **303**, 60–68.
72 Z. Kozakova, I. Kuritka, N. E. Kazantseva, V. Babayan, M. Pastorek, M. Machovsky, P. Bazant and P. Saha, *Dalton Trans.*, 2015, **44**, 21099–21108.
73 I. Fernández-Barahona, M. Muñoz-Hernando and F. Herranz, *Molecules*, 2019, **24**, 1224.
74 A. Shibatani, H. Kan, Y. Asakuma and A. Saptoro, *Cryst. Res. Technol.*, 2020, **55**, 1900199.
75 K. Martina, S. Tagliapietra, A. Barge and G. Cravotto, *Top. Curr. Chem.*, 2016, **374**, 79.
76 J. Ma, G. a. Tai and W. Guo, *Ultrason. Sonochem.*, 2010, **17**, 534–540.
77 Z. Jiao, Y. Zhang and H. Fan, *J. Chromatogr. A*, 2016, **1457**, 7–13.
78 R. Dolores, S. Raquel and G.-L. Adianez, *Ultrason. Sonochem.*, 2015, **23**, 391–398.
79 A. Soltani and P. Pakravan, *Adv. Pharmaceut. Bull.*, 2023, **13**, 301–308.
80 M. Muthiah, I.-K. Park and C.-S. Cho, *Biotechnol. Adv.*, 2013, **31**, 1224–1236.
81 F. Trotta, K. Martina, B. Robaldo, A. Barge and G. Cravotto, *J. Inclusion Phenom. Macrocycl. Chem.*, 2007, **57**, 3–7.
82 K. Martina, F. Trotta, B. Robaldo, N. Belliardi, L. Jicsinszky and G. Cravotto, *Tetrahedron Lett.*, 2007, **48**, 9185–9189.
83 A. Goodarzi, Y. Sahoo, M. T. Swihart and P. N. Prasad, *MRS Online Proc. Libr.*, 2003, **789**, 23.
84 Z. Shaterabadi, G. Nabiyouni and M. Soleymani, *Mater. Sci. Eng., C*, 2017, **75**, 947–956.
85 K. Martina, F. Baricco, G. Berlier, M. Caporaso and G. Cravotto, *ACS Sustain. Chem. Eng.*, 2014, **2**, 2595–2603.
86 Y. S. Li, J. S. Church, A. L. Woodhead and F. Moussa, *Spectrochim. Acta, Part A*, 2010, **76**, 484–489.
87 A. Qureashi, A. H. Pandith, A. Bashir, T. Manzoor, L. A. Malik and F. A. Sheikh, *Surface. Interfac.*, 2021, **23**, 101004.
88 H.-C. Kim, E. Kim, S. W. Jeong, T.-L. Ha, S.-I. Park, S. G. Lee, S. J. Lee and S. W. Lee, *Nanoscale*, 2015, **7**, 16470–16480.
89 M. Răcuciu, D. E. Creangă and A. Airinei, *Eur. Phys. J. E*, 2006, **21**, 117–121.
90 G. Liu, R. Y. Hong, L. Guo, Y. G. Li and H. Z. Li, *Appl. Surf. Sci.*, 2011, **257**, 6711–6717.
91 H. K. Can, S. Kavlak, S. ParviziKhosroshahi and A. Güner, *Artif. Cells, Nanomed. Biotechnol.*, 2018, **46**, 421–431.
92 S. Ghosh, A. Z. M. Badruddoza, M. S. Uddin and K. Hidajat, *J. Colloid Interface Sci.*, 2011, **354**, 483–492.

93 C. E. Sjögren, C. Johansson, A. Nævestad, P. C. Sontum, K. Briley-Sæbø and A. K. Fahlvik, *Magn. Reson. Imag.*, 1997, **15**, 55–67.
94 Y. Zhang, L. Zhang, X. Song, X. Gu, H. Sun, C. Fu and F. Meng, *J. Nanomater.*, 2015, **2015**, 417389.
95 Á. Buvári, L. Barcza and M. Kajtár, *J. Chem. Soc., Perkin Trans. 2*, 1988, 1687–1690, DOI: 10.1039/P29880001687.
96 K. Martina, F. Baricco, G. Berlier, M. Caporaso and G. Cravotto, *ACS Sustainable Chem. Eng.*, 2014, **2**, 2595–2603.
97 J.-W. Wang, K.-X. Yu, X.-Y. Ji, H. Bai, W.-H. Zhang, X. Hu and G. Tang, *Molecules*, 2021, **26**, 2412.
98 H. Sharifi Dehsari, V. Ksenofontov, A. Möller, G. Jakob and K. Asadi, *J. Phys. Chem. C*, 2018, **122**, 28292–28301.
99 I. S. Elashmawi and H. M. Alhusaiki-Alghamdi, *Opt. Quant. Electron.*, 2024, **56**, 1090.
100 X. Sun, C. Zheng, F. Zhang, Y. Yang, G. Wu, A. Yu and N. Guan, *J. Phys. Chem. C*, 2009, **113**, 16002–16008.
101 A. Roch, R. N. Muller and P. Gillis, *J. Chem. Phys.*, 1999, **110**, 5403–5411.
102 L. Bordonali, T. Kalaivani, K. P. V. Sabareesh, C. Innocenti, E. Fantechi, C. Sangregorio, M. F. Casula, L. Lartigue, J. Larionova, Y. Guari, M. Corti, P. Arosio and A. Lascialfari, *J. Phys.: Condens. Matter*, 2013, **25**, 066008.
103 Y. Svenskaya, F. Garello, E. Lengert, A. Kozlova, R. Verkhovskii, V. Bitonto, M. R. Ruggiero, S. German, D. Gorin and E. Terreno, *Nanotheranostics*, 2021, **5**, 362–377.
104 M. Ghasemi, T. Turnbull, S. Sebastian and I. Kempson, *Int. J. Mol. Sci.*, 2021, **22**, 12827.